ACS APPLIED ENERGY MATERIALS

www.acsaem.org
Article

Enhancing Electrocatalysis: Engineering the Fe–N_x–C Electrocatalyst for Oxygen Reduction Reaction Using Fe-Functionalized Silica Hard Templates

Mohsin Muhyuddin,[‖] Silvia Mostoni,[‖] Hilah Clara Honig,[‖] Lorenzo Mirizzi, Lior Elbaz, Roberto Scotti, Massimiliano D'Arienzo,* and Carlo Santoro*

Cite This: https://doi.org/10.1021/acsaem.4c01215

ABSTRACT: The availability of robust and accessible active sites in iron–nitrogen-carbon (Fe–N_x-C) electrocatalysts is essential to optimize the oxygen reduction reaction (ORR), which is the main obstacle in the commercial realization of fuel cells. Herein, a modified hard templating method to develop efficient Fe–N_x-C has been presented that not only ensured the generation of a porous architecture but also helped in the homogeneous distribution of Fe throughout the structure. First, silica nanoparticles (NPs) were grown via the Stöber process and then functionalized atomically with iron through two different types of silane chains, i.e., (3-aminopropyl)triethoxysilane (APTES) and N-(2-Aminoethyl)-3-aminopropyltriethoxysilane (EDTMS). The Fe-functionalized silica simultaneously acting as a sacrificial template as well as an iron source was then impregnated with nicarbazin, which was a carbon and nitrogen precursor. The dried mix was subject to pyrolysis (H1) followed by acid washing to dissolve silica templates, and then, again, it was subjected to another pyrolysis treatment (H2). At each proceeding step, ORR activity in both acidic and alkaline media was improved and the samples obtained at the last stage (i.e., H2) outperformed the other counterparts collected at the initial stages of the fabrication pathway. Eventually, the electrocatalyst developed using EDTMS-type silane attached to silica NPs (E_FeNC_H2) demonstrated the highest onset potentials of 990 mV vs RHE in alkaline media and 862 mV vs RHE in acidic media. Moreover, the lower peroxide yield of E_FeNC_H2 signifying nearly direct 4e^- ORR was attributed to the highest specific surface area (627 m^2 g^{-1}) and the optimum combination of active moieties dispersed in the porous carbonaceous framework.

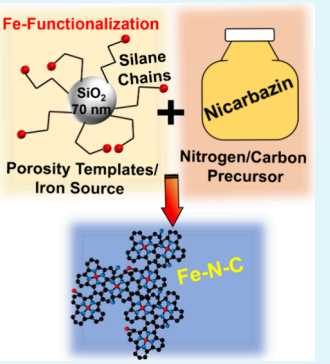

KEYWORDS: *oxygen reduction reaction, single atom electrocatalyst, Fe–N–C, functionalized silica templates, sacrificial support method, PGM-free electrocatalyst*

INTRODUCTION

To alleviate the existing energy crisis and address associated environmental concerns, the methods of energy production and consumption need to be modernized, considering sustainability as the primary goal. In such a scenario, low-temperature fuel cells being green and clean energy technologies are acquiring the attention of academic and industrial sectors, since they demonstrate remarkable potential for sustainable applications in both mobile and stationary settings. The energy generation mechanism of most fuel cells is based on the hydrogen oxidation reaction (HOR) and oxygen reduction reaction (ORR) occurring at the anode and cathode, respectively. Contrary to the anode side reaction, the ORR is thermodynamically complex and kinetically sluggish, as it involves difficult oxygen activation/adsorption and passes through a complicated reaction pathway. To improve the reaction kinetics while maintaining the complete reduction of oxygen with water as the final product, a significant amount of Pt-based electrocatalyst is required, which can be up to 8 times more in quantity in the fuel cell anode.[1] Therefore, the cathode singularly consumes approximately 80% of the total Pt-based electrocatalyst which accounts for 56% of the membrane electrode assembly (MEA) cost.[2,3] On the other hand, skyrocketing prices and the scarcity of platinum group metals (PGMs) challenge the commercial feasibility of fuel cells. Moreover, instability and operational deterioration of PGM electrocatalysts economically jeopardize the U.S. Department of Energy's set cost target of US$30 per kW for the transportation sector.[4] In this regard, the transition from the relatively mature class of proton-exchange membrane fuel cells (PEMFCs) to anion-exchange membrane fuel cells (AEMFCs) can provide an opportunity to replace PGMs with cost-effective transition metal (TM)-based electrocatalysts due to

Received: May 11, 2024
Revised: October 28, 2024
Accepted: November 4, 2024

the lowered leverage of the corrosion conditions. TM-based PGM-free electrocatalysts are not new to the scientific community as Jasinski pioneered this field by reporting cobalt phthalocyanine as a molecular electrocatalyst for ORR in the alkaline electrolyte.[5] Henceforth, a new frontier of PGM-free TM-based electrocatalysts has been evolved.[6−8] Among various sorts of TM-based ORR electrocatalysts, iron−nitrogen-carbon (Fe−N_x-C) has emerged as a reliable candidate. The extraordinary electrocatalytic activity of Fe−N_x-C is attributed to the optimum electronic density and interaction of iron with oxygen, especially when the iron is present in coordination with nitrogen at the atomic level which helps in the binding and subsequent reduction of oxygen.[9]

Over the last few decades, significant research has been conducted in the arena of Fe−N_x-C but still, the electrocatalytic performance lags behind the state-of-the-art PGM-based electrocatalysts. One of the major bottlenecks is the inefficacious architectural design of Fe−N_x-C where the abundance of active sites with maximum accessibility is the key parameter to ensure higher activity and selectivity.[10−13] Fe−N_x-C electrocatalysts are composed of numerous types of active sites containing Fe, such as Fe−N_4, and metal-free sites such as N-graphitic, N-pyridinic, N-pyrrolic, N-oxides, and others. These active sites contribute differently to ORR: (i) Fe−N_4, contributes to the direct 4 electron transfer, (ii) nitrogen moieties contribute to the two-electron transfer (O_2 to intermediate), (iii) nitrogen-pyridinic active site contributes to the reduction of the intermediate to the final product.[9,14,15] Therefore, while engineering the active site structure of Fe−N_x-C, the primary task is to multiply the most active and robust active moieties such as FeN_4, pyridinic, and hydrogenated nitrogen[9,14−17] and thus a structure having "in-plane" and "edge" active sites with atomic level dispersion.[18] In addition to Fe−N_4, different symmetries for instance an extra-axial nitrogen ligand attached to Fe−N_4 and binary sites, i.e., Fe_2N_5 have also been observed.[19,20] Moreover, metallic nanoparticles of iron oxide[21] and iron carbide[22] have also been reported as additional active sites for alkaline media. Nevertheless, if the aforementioned active moieties are inaccessible, they will not actively participate in the ORR.[23] Fe−N_x-C is typically synthesized by pyrolysis at higher temperatures, and therefore, the production of porous architecture becomes inevitable.[24,25] Kramm and co-workers methodically clarified the origin of the improved electrocatalytic activity in the Fe−N_x−C pyrolyzed under different conditions, i.e., Ar and Ar + NH_3.[26] They concluded that the higher activity of Ar + NH_3 pyrolyzed Fe−N_x-C could be attributed to readily available active sites whereas in the Ar-type Fe−N_x−C, the majority of active sites were isolated within the material and remained unavailable. Jaouen et al. argued that the overall activity of the electrocatalyst is controlled by the micropores per unit mass when the adequate level of nitrogen is atomically integrated into the carbon framework and the active site is a molecular assembly that bridges the two-pore walls.[27] Similarly, Kim et al. elucidated the role of predefined microporosity in finding the active sites in Fe−N−C while maximizing Fe−N_x to ensure optimum ORR activity.[28] In contrast, narrower micropores can restrict the internal diffusion within the electrocatalyst and limit the accessibility of the active moieties.[29] Some coordinations of Fe and N are usually located in the micropores that undergo limited oxygen diffusion along with flooding problems during working and may also cause imperfect impregnation with ionomers.[30] However, the mesopores guarantee enhanced ORR activity and improved mass transport.[31] Considering such challenges, Han and co-workers, attempted to engineer a hollow mesoporous nanoarchitecture with atomically dispersed active sites that ensured higher electrocatalytic performance.[32] Recently, Mazzucato et al. clarified that both micro and mesopores are important while stressing that microporosity must be accompanied by sufficient mesoporosity to avoid flooding and capillary condensation within the micropores.[33]

To induce finely dispersed and interconnected micro-mesoporosity in the Fe−N−C, the sacrificial support method (SSM) is a well-established technique in which hard templates, i.e., silica nanoparticles (NPs) are used and after pyrolysis, they are removed by acidic etching to create a well-defined porous structure.[34] This method is the one used by Pajarito Powder to synthesize the only commercially available Fe−N_x−C electrocatalyst.[35] Different other templating agents have also been researched.[36,37] Soft templating techniques are also very popular synthetic methods in which self-assembled surfactants are often used as pore-inducing agents.[38] However, this method has limitations concerning narrow pore sizes and insufficient pore volumes.[39] During pyrolysis, another problem encountered is the coalescence of the iron species into iron oxide and carbide NPs at elevated temperatures that severely reduce the electrocatalytic activity due to the blockage of transportation channels and also affect the stability of the derived Fe−N_x−C type electrocatalysts.[40−43] Moreover, Mathur et al. identified that the choice of nitrogen precursor also impacts the final activity of the electrocatalysts.[44] Among many nitrogen precursors, Nicarbazin is considered a very important charge-transfer organic salt that undergoes melting during pyrolysis and helps in homogenization and porosity increase.[34,45] Very recently, the synthesis of ORR electrocatalysts based on the mixture of Nicarbazin, silica NPs and iron nitrate was revealed through several in situ microscopic and spectroscopic techniques.[45] On the other hand, Kübler et al. functionalized carbon nanotubes with iron acetate and phenanthroline via indazole or pyridine, resulting in an efficient Fe−N_x−C electrocatalyst for acidic media.[46]

Herein, we report a novel strategy to launch porous architecture in Fe−N_x−C electrocatalysts with accessible and reactive single-atom-based active sites by exploiting a tailored sacrificial support strategy. Particularly, as the traditional methods reported in the literature, the three necessary components, nicarbazin, iron sources, and silica template are mixed mechanochemically before being pyrolyzed, leading to statistically dispersed iron over the entire mixture. Interestingly, in the present study, Fe and N are integrated over the silica by directly anchoring the Fe active centers to the NPs through aminosilane chains before mixing with Nicarbazin, enabling fine control of the metal dispersion and distribution. A systematic research design was commenced first involving the synthesis of silica NPs and subsequent functionalization of the synthesized silica NPs with Fe using two different types of silane ligands which ensure atomically and homogeneously dispersed metal centers. Next, the Fe-functionalized silica NPs were separately impregnated with nicarbazin which acted as a carbon and nitrogen source. The dried sludge was subjected to temperature-controlled pyrolysis followed by acid etching to remove completely the silica NPs template, to produce a porous Fe−N_x−C active structure. Lastly, another pyrolysis treatment in a reducing atmosphere was given to improve graphitization and clean up the Fe−N_x active sites. The

https://doi.org/10.1021/acsaem.4c01215
ACS Appl. Energy Mater. XXXX, XXX, XXX−XXX

physicochemical and electrochemical characteristics of Fe−N−C samples collected at each fabrication step were thoroughly analyzed with advanced characterization tools. The given study conceivably emphasizes the outcomes of thoughtful synthesizing and engineering of PGM-free Fe−N_x−C electrocatalysts on the progress of sustainable and clean energy applications.

MATERIALS AND METHODS

Materials. All chemicals used in this work were of high-purity analytical grade, and they were used without any further processing. For the synthesis of iron functionalized silica NPs, tetraethylorthosilicate (TEOS), ammonium hydroxide (NH_4OH 25%), and iron sulfate heptahydrate $Fe_2(SO_4)_3{\cdot}7H_2O$ were purchased from Merck Life Science. (3-Aminopropyl)triethoxysilane (APTES) and N-(2-Aminoethyl)-3-aminopropyltriethoxysilane (EDTMS) were purchased from abcr Gute Chemie. Ethanol (EtOH) 99.8% was obtained from Exacta Optech LabCenter. For the electrocatalyst preparation, nicarbazine (NC) was acquired from Merck Life Science.

Synthesis of Silica Templates. Iron species were dispersed on the surface of the SiO_2 NPs. Briefly, SiO_2 NPs (70 ± 5 nm average diameter) were synthesized through a classical Stöber procedure, by the condensation of TEOS in a basic ethanol solution.[47,48] After recovering, APTES or EDTMS were anchored onto the surface of SiO_2 NPs through their hydrolysis and condensation reactions with the surface −OH groups available onto the silica NPs, using a silane:OH groups molar ratio equal to 1:2.[49] These surface ligands were exploited both as nitrogen sources and to promote iron coordination and dispersion. The samples are herein called Si_A or Si_E respectively, where "A" and "E" mean APTES or EDTMS. In the last step, iron species were dispersed onto the surface of SiO_2 NPs by adding $Fe_2(SO_4)_3{\cdot}7H_2O$, using a Fe:silane molar ratio equal to 1.5:1 to maximize the amount of iron on the SiO_2 surface (functionalization with APTES and EDTMS were realized in toluene at 120 °C while the iron dispersing is done in ethanol at reflux conditions). The final material was recovered through centrifugation, washed with fresh EtOH, dried at 80 °C overnight, and finally labeled as Si_AFe and Si_EFe, respectively.

Electrocatalysts Synthesis. Using Fe-functionalized silica NPs via APTES and EDTMS, named as Si_AFe and Si_EFe respectively, Fe−N_x−C electrocatalysts were methodologically synthesized. It is important to note that Si_AFe and Si_EFe acted as hard templates to induce porosity as well as Fe precursor in which Fe is already present atomically on the silica surface. Here NC was used as an organic source of nitrogen and carbon and was mixed with Si_AFe or Si_EFe in a 7:3 mass ratio. The mixture was blended with Milli-Q water for 24 h under nonstop stirring at room temperature (RT). Afterward, the mixture was dried in the oven at 80 °C, and the obtained material was pulverized into a fine powder and subjected to pyrolysis. The first pyrolysis (H1) was carried out at 900 °C under pure Ar for 1 h where the heating and cooling rates were maintained at 5 °C min^{-1}. The samples collected at this step were labeled A_FeNC_H1 (when Si_AFe was used) and E_FeNC_H1 (when Si_EFe was used). In the next step, the samples were etched with an acidic solution (1:2 mixture of 35 wt % HNO_3 and 25 wt % HF) for 3 days to eliminate the silica NPs while leaving a porous network behind, and the achieved samples were called A_FeNC_E and E_FeNC_E. Subsequently, the dried samples from the last step were again pyrolyzed (H2) under a slightly reducing atmosphere of N_2/H_2 95/5 wt % whereas the other conditions remained similar to H1. The final sample was labeled as A_FeNC_H2 or E_FeNC_H2 depending on the initial type of functionalized silica used. The electrocatalysts developed at different stages of the experimental pathway are summarized in Table S1.

Structural and Morphological Characterization. Attenuated total reflectance (ATR) infrared spectroscopy (FTIR) was performed with a Thermo Fisher Scientific Nicolet iS20 instrument (wavenumber range 4000−550 cm^{-1}, resolution 4 cm^{-1}, 32 scans). FTIR spectra were recorded on the as-prepared Si_AFe and Si_EFe, after mixing with nicarbazin and after each step of the electrocatalyst preparation. The absorbance spectra of the SiO_2 NPs before and after functionalization were acquired utilizing the double-beam UV−visible spectrophotometer "Lambda 950" from PerkinElmer, equipped with an integrating sphere, enabling the analysis of solid-state samples.

Thermogravimetric analysis (TGA) was carried out by using a Mettler Toledo StarE system TGA/DSC1 (scan range of 30−1000 °C, heat rate of 10 °C min^{-1}, and airflow of 50 mL min^{-1}). The following samples were analyzed: the as-prepared Si_AFe and Si_EFe NPs to confirm the silica functionalization with APTES and EDTMS, and the final electrocatalyst obtained after the whole preparation procedure to verify the effective absence of silica NPs (Figure S1). The iron amount was measured with the inductively coupled plasma-optical emission spectroscopy (ICP-OES), using an ICP-OES Optima 7000 DV PerkinElmer instrument. The acid digestion was realized in a microwave Milestone Ethos mineralizer instrument. X-ray powder diffraction (XRPD) was conducted with a Rigaku MiniFlex 600 diffractometer with 0.154 nm Cu Kα radiation, in the 2θ range 5−80° (2θ step 0.02°, 1° min^{-1} scan rate). The carbon structures of the fabricated samples were analyzed via Raman spectroscopy (Jasco Ventuno μ-Raman system) using a He−Ne laser with a wavelength of 632.8 nm and a power density of 6 kW cm^{-2}. The Peltier-cooled charge-coupled device (CCD) camera was operated at −50 °C. The equipment was calibrated using a standard reference peak of a silicon single crystal at 520.65 cm^{-1}. BET measurements were conducted using a Quantachrome Autosorb iQ instrument with nitrogen as the adsorbate at 77 K. The pore size distribution was calculated using the DFT method for slit pores. X-ray photoelectron spectroscopy (XPS) analysis was conducted using a Nexsa spectrometer equipped with a monochromatic, microfocused, lower Al Ka X-ray (photon energy 1486.6 eV). Further investigation of the morphological structure of the catalysts was done by using high-resolution transmission electron microscopy (HRTEM), JEOL JEM 2100, LaB6 filament, 200 kV.

Electrochemical Measurements. The ORR electrocatalytic activities of the samples were studied by using a classical three-electrode system based on the Pine WaveVortex RDE attached to a Pine bipotentiostat. To configure the working electrode, first, the electrocatalyst ink was prepared using previously reported methods.[50−52] Briefly, 5 mg of the sample was added to the mixture of isopropanol (985 μL) and 5 wt % Nafion D-520 binder (15 μL) and subjected to sonication for 30 min until a homogeneous ink was obtained. Then, the estimated volume (for 0.6 mg cm^{-2} electrocatalyst loading) of the prepared ink was dropcasted on the glassy carbon disk of the rotating ring disk electrode (RRDE) and dried at room temperature. The RRDE (E6R2 series) had a disk surface area of 0.2376 cm^2 whereas the collection efficiency (N) and area of the Pt ring (used for the detection of peroxide formed during ORR) were 38% and 0.2356 cm^2, respectively. In this study, the counter electrode was comprised of a graphite rod whereas for the reference saturated calomel electrode (SCE, $E°_{SCE}$ = 241 mV vs SHE) was utilized to complete the cell. All the potentials presented in the given study were converted to a reversible hydrogen electrode (RHE) using eq 1.

$$E(\text{vs RHE}) = E(\text{vs SCE}) + E°_{SCE} + (0.0591 \times \text{pH}) \quad (1)$$

The ORR measurements were performed in O_2-saturated 0.5 M H_2SO_4 and 0.1 M KOH while keeping the rotation rate of RRDE at 1600 rpm in the potential window of 1.1 to −0.2 V vs RHE. The potential of the Pt ring was kept constant at 1.2 V vs RHE. Before recording the actual measurements, the deposited electrocatalyst on RRDE was activated in the electrolyte by obtaining a few cyclic voltammograms (CVs) at 50 mV s^{-1} scan rate while waiting for a stable current to be achieved. Then CVs (at a scan rate of 5 mV s^{-1}) under stationary conditions were acquired (in the alkaline media). Ultimately, linear sweep voltammograms (LSVs) at 5 mV s^{-1} were recorded and then by measuring the disk (I_{disk}) and ring (I_{ring}) currents, peroxide production (%) and the number of electrons transferred during ORR (n) were calculated using eqs 2 and 3, respectively.

https://doi.org/10.1021/acsaem.4c01215
ACS Appl. Energy Mater. XXXX, XXX, XXX−XXX

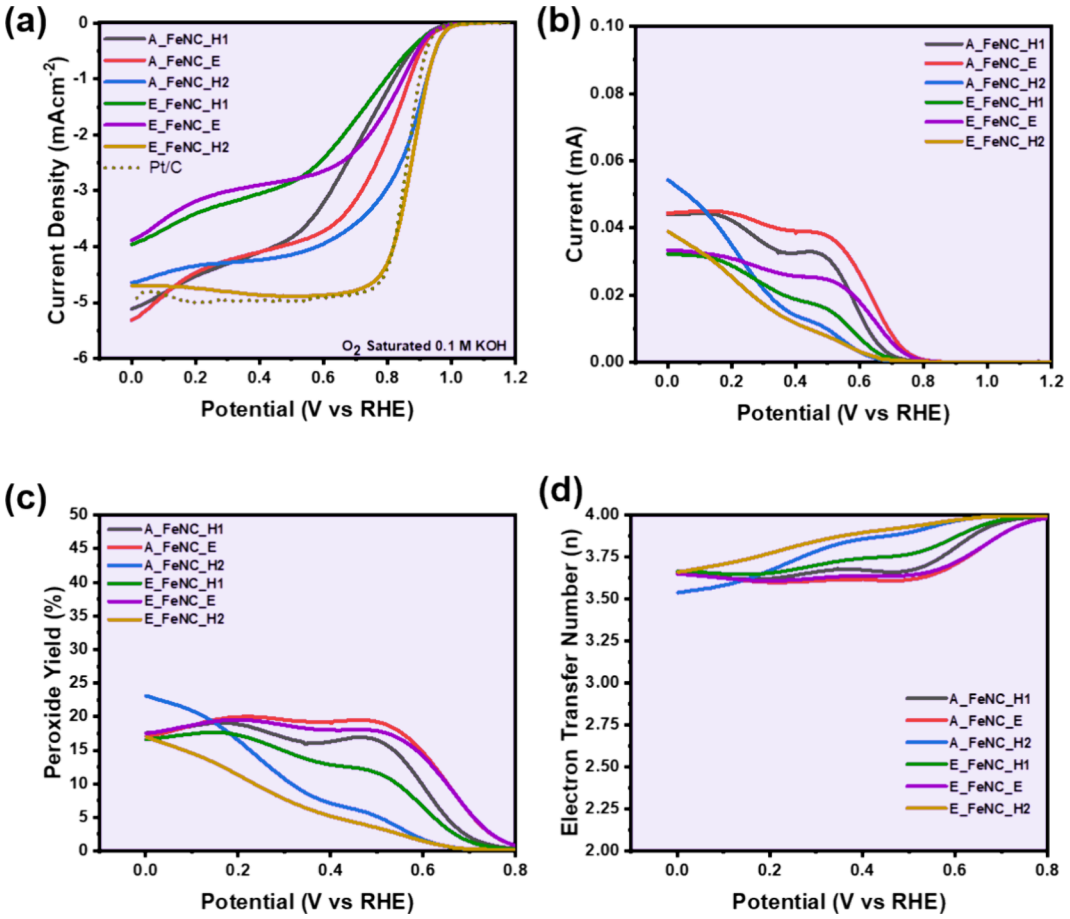

Figure 1. ORR in O_2-saturated 0.1 M KOH with 0.6 mg cm^{-2} electrocatalysts loading on RRDE rotating at 1600 rpm; (a) LSVs recorded at 5 mV s^{-1}, (b) ring current trends, (c) peroxide yield, and (d) electron transfer number as a function of potential. For comparison, the benchmark Pt/C with a typical loading of 30 μgPt cm^{-2} was also analyzed under the same conditions, and the LSV was plotted with dotted lines.

$$\text{Peroxide (\%)} = \frac{200 \times \frac{I_{ring}}{N}}{I_{disk} + \frac{I_{ring}}{N}} \quad (2)$$

$$n = \frac{4I_{disk}}{I_{disk} + \frac{I_{ring}}{N}} \quad (3)$$

To compare the electrocatalytic activity, commercially available 40 wt % Pt supported on carbon (Pt/C) was used as a benchmark electrocatalyst and the loading on RRDE was kept at 30 μgPt cm^{-2}.

RESULTS AND DISCUSSION

Fe−N_x−C ORR electrocatalysts were developed by using the modified hard templating method in which Fe-functionalized silica acted as a pore-forming agent as well as a Fe source that can help in restricting the coalescence of Fe in mass-scale NPs. NC was exploited as a source of carbon and nitrogen combined with Si_AFe and Si_EFe templates to achieve a high iron dispersion into the carbon matrix and demonstrate the high versatility of this procedure which can be applied to different carbon-based precursors. The UV−visible spectra provided in Figure S2 indicated a considerable increase in the absorbance of the functionalized SiO_2 templates, i.e., Si_AFe and Si_EFe compared to the pristine SiO_2 NPs. The effective functionalization with silanes and iron onto the SiO_2 surface in Si_AFe and Si_EFe was assessed by FTIR, TGA, and ICP-OES analyses (not reported). Si_AFe is composed of 92.2 wt % of SiO_2, 6.4 ± 0.3 wt % of APTES and 1.4 wt % ± 0.1 of Fe, whereas Si_EFe consists of 92.6 wt % of SiO_2, 5.9 ± 0.2 wt % of EDTMS and 1.5 wt % ± 0.1 of Fe.

The electrocatalytic activities of Fe−N_x−C samples obtained at each step of the synthesis were analyzed in alkaline and acidic media to evaluate the efficacy of the adopted fabrication strategy. To start with, cyclic voltammograms under stationary conditions were acquired in an O_2-saturated alkaline media (0.1 M KOH) on each sample as reported in Figure S3. Interestingly, all the samples exhibited an intense reduction peak that not only became sharper but also shifted to the right as the fabrication steps progressed, indicating an enhancement in electrocatalytic performance. Subsequently, RRDE measurements were conducted in 0.1 M KOH with a rotation speed of 1600 rpm, and the obtained trends are illustrated in Figure 1. Similarly, the performance continued to enhance as the synthesis and processing pathway proceeded. From the recorded LSVs (Figure 1a), the samples obtained after the first pyrolysis, i.e., A_FeNC_H1 and E_FeNC_H1, had the lowest ORR activity with higher ORR overpotentials. The onset potential (E_{onset}) taken at 0.1 mA cm^{-2} is 0.945 and 0.956 V vs RHE for A_FeNC_H1 and E_FeNC_H1, respectively. Interestingly, when the samples were etched with an acidic solution to dissolve silica NPs, the activity was considerably enhanced with a clear improvement in the E_{onset} and half-wave potentials ($E_{1/2}$). Whereas the samples obtained at the final stage of the second pyrolysis under a slightly reducing atmosphere demonstrated the highest E_{onset} of ca.

https://doi.org/10.1021/acsaem.4c01215
ACS Appl. Energy Mater. XXXX, XXX, XXX−XXX

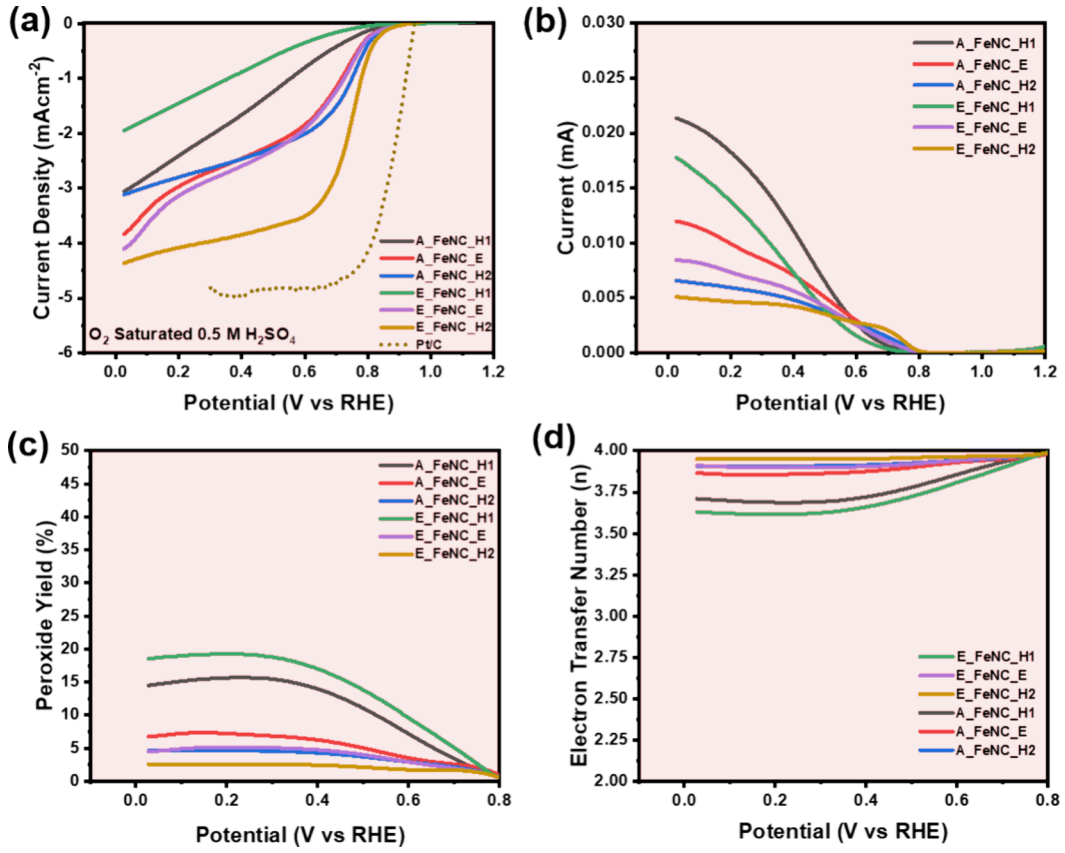

Figure 2. ORR in O_2-saturated 0.5 M H_2SO_4 with 0.6 mg cm^{-2} electrocatalysts loading on RRDE rotating at 1600 rpm; (a) LSVs recorded at 5 mV s^{-1}, (b) ring current trends, (c) peroxide yield and (d) electron transfer number as a function of potential. For comparison, the benchmark Pt/C with a typical loading of 30 μgPt cm^{-2} was also analyzed under the same conditions and the LSV was plotted with dotted lines.

0.986 and 0.990 V vs RHE, for A_FeNC_H2 and E_FeNC_H2, respectively. However, the latter sample showed a relatively higher limiting current density ($J_{limiting}$). To make a comparison, the electrocatalytic activity of commercial Pt/C was also analyzed under similar conditions. E_FeNC_H2 showed E_{onset} and $E_{1/2}$ higher than that of Pt/C, however, the $J_{limiting}$ was slightly lower. Recently, Chen et al. formulated a comprehensive investigation using in situ and ex-situ techniques to trace the basis of activity enhancement during the second pyrolysis.[53] They observed that the improvement in the activity is due to increased homogenization of the active moieties, particularly Fe−N_x sites while avoiding the coalescence of Fe into metallic NPs and preserving the morphological integrity of the carbonaceous matrix during the first pyrolysis stage. In addition to activity, selectivity is another criterion to examine the practicality of the electrocatalysts. For fuel cell application, the direct four-electron pathway is inevitably important and hence the peroxide production should be as low as possible. By virtue of the Pt ring around the glassy carbon disk of the RRDE, the extent of peroxide production can be synchronically estimated, where the recorded ring currents across the monitored potential window are demonstrated in Figure 1b. The peroxide anion yield during ORR in the alkaline media can be seen in the third panel (Figure 1c), indicating different trends in peroxide generation for the samples obtained at different stages. The samples collected at the initial two steps i.e., the first pyrolysis and acid etching showed a steady ascent in the peroxide yield as the overpotential increased. However, after showing a nearly constant behavior, the peroxide yield tended to decrease at very high overpotentials, indicating the 2 + 2 e^- reduction route of oxygen on these electrocatalysts. It has been observed previously that the peroxide produced at the primary active sites can be subsequently reduced to water at the secondary active sites in a stepwise reduction.[9,14] Notably, the peroxide yield with the electrocatalysts collected after the second pyrolysis, i.e., A_FeNC_H2 and E_FeNC_H2 exhibited a dissimilar tendency, exhibiting a substantial reduction in the peroxide yield. Although it tended to increase as the overpotential proceeded, the peroxide generation with E_FeNC_H2 reliably remained below 20%. Next, the electron transfer number (Figure 1d) always remained above 3.5 whereas A_FeNC_H2 and E_FeNC_H2 exhibited nearly four-electron ORR.

Although Fe−N_x−C type electrocatalysts are particularly important for the AEMFCs due to reduced corrosion conditions, their electrocatalytic activity was also evaluated in an acidic medium (0.5 M H_2SO_4) to mimic the ORR in PEMFCs and the obtained trends are demonstrated in Figure 2. Overall ORR tendency remained consistent with that exhibited in 0.1 M KOH. However, the E_{onset} and $E_{1/2}$ were slightly reduced in comparison with those under the alkaline conditions. The activity parameters, i.e., E_{onset} and $E_{1/2}$ have been summarized in Table S2. During ORR in 0.5 M H_2SO_4, E_FeNC_H2 again outperformed the other counterparts with the highest E_{onset} of 0.862 V vs RHE whereas A_FeNC_H2 exhibited a marginally lower E_{onset} of 0.847 V vs RHE. (Figure 2a) It is well-known that electrocatalysts show relatively lower

https://doi.org/10.1021/acsaem.4c01215
ACS Appl. Energy Mater. XXXX, XXX, XXX−XXX

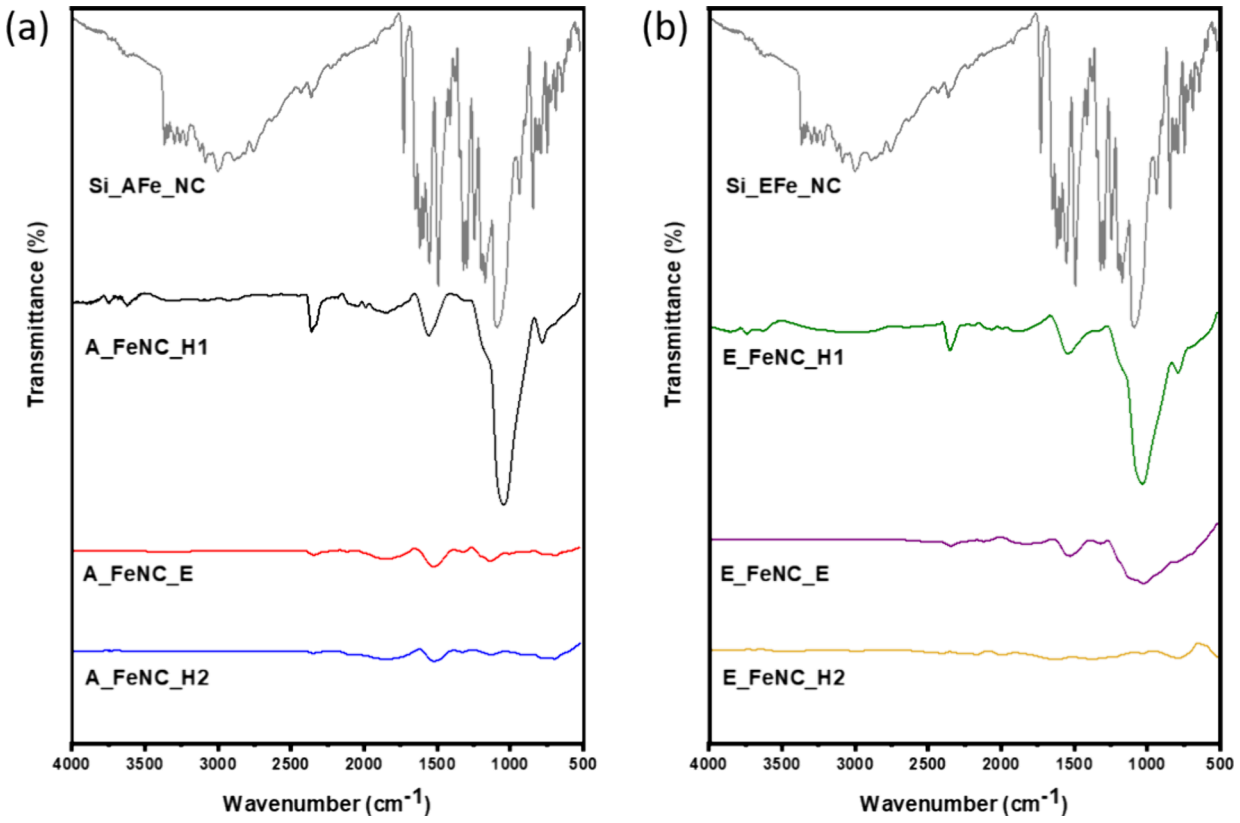

Figure 3. FTIR spectra of the as-prepared samples at each stage of the electrocatalyst experimental design. (a) FTIR spectra of the samples fabricated via Si_AFe-type templates, whereas (b) samples involved Si_EFe-type templates during synthesis.

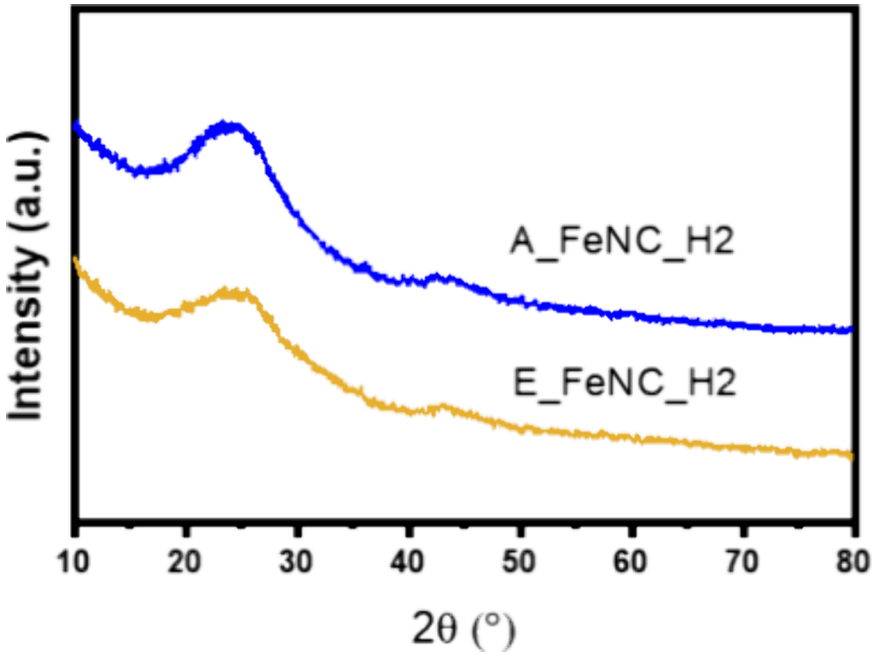

Figure 4. XRPD spectra of A_FeNC_H2 and E_FeNC_H2.

E_{onset} and $E_{1/2}$ in acidic media compared to their corresponding values in alkaline media.[15,54,55] One possible reason could be that at extremely low pH the rate-determining step does not depend on the H^+ concentration; however, at higher pH, the rate-determining step involves the first electron transition.[55] Moreover, the anionic peroxide that forms in the alkaline electrolyte stabilizes on the iron sites and contributes to the $E_{1/2}$ which is unlikely under acidic conditions. Interestingly, in acidic media, the peroxide production was further decreased (Figure 2c). Compared to the samples achieved after the first pyrolysis stage (H1), the subsequent samples showed a very low peroxide yield, where the E_FeNC_H2 peroxide was restricted to a maximum of ca. 2.5% throughout the potential window. The electron transfer number provided in Figure 2d

https://doi.org/10.1021/acsaem.4c01215
ACS Appl. Energy Mater. XXXX, XXX, XXX−XXX

clearly shows direct four-electron ORR in the acidic solution. Conversely, slightly higher peroxide production in the alkaline media can be linked with the adsorption of hydroxide species that not only restrict the oxygen adsorption but also encourage the outer-sphere-electron transfer route, causing bielectronic oxygen electro-reduction with a generation of peroxide as an intermediate product.[56] However, the ORR kinetics of E_FeNC_H2 in acidic media still remains lower than the benchmark Pt/C electrocatalyst.

To ascertain the origin of the electrocatalytic activity, the structural attributes of the obtained samples were systematically studied. Starting with the material characterization, FTIR analysis was carried out after each preparation step of the electrocatalyst (Figure 3). The typical spectrum of NC is evident after mixing both Si_AFe and Si_EFe with NC, but the first pyrolysis treatment (H1) is responsible for its degradation, thus leading to the appearance of the typical spectrum of SiO_2 NPs, dominated by the main peak at 1100 cm^{-1} due to Si−O−Si stretching. The gradual disappearance of this peak in A_FeNC_E and E_FeNC_E, as well as its complete annihilation in A_FeNC_H2 and E_FeNC_H2 samples, suggests the successful silica removal through the etching treatment. This was further confirmed by TGA analyses performed on the final samples (Figure S1) where no inorganic residues were detected at the end of the analyses (1000 °C) and the complete combustion of the organic component due to the formed carbon matrix was measured. Moreover, the peak at 1570 cm^{-1} may correspond to the NH_2 scissor vibration of the surface ligands.[57]

Next, the crystallographic features of the electrocatalysts were investigated with XRPD, and the obtained diffraction patterns are reported in Figures 4 and S5. For the samples obtained at the last stage of the fabrication route, i.e., A_FeNC_H2 and E_FeNC_H2, only a broader band due to amorphous carbon can be observed at ca. 24.5° and one minor peak at about 44° that can be ascribed to 002-oriented and 101-oriented graphitic diffractions, respectively, signifying defective and amorphous carbon.[58] These peaks become more evident after the etching procedure which allows in principle the complete removal of the silica templates and the weakening of the corresponding broader band at 22°, mainly visible after the first pyrolysis (H1) and the degradation of the NC structure (Figure S5, A_FeNC series reported as representative sample). Notably, the final samples did not show any diffraction peak consistent with Fe NPs or iron segregated phases, such as oxide and/or carbides, endorsing the atomic level distribution of Fe species without mass scale coalescence.[59,60] Moreover, to examine the evolved graphitic structures of the electrocatalysts, Raman spectroscopy was employed, and the achieved spectra have been demonstrated in Figure S6. The acquired spectra exhibited typical 'D' and 'G' bands at nearly ca. 1340 and 1580 cm^{-1}, respectively, The D band indicates the structural defects present in the carbon framework whereas the G band corresponds to graphitization and the I_D/I_G ratio serves as a common indicator to estimate the defect density of the carbonaceous materials. Interestingly, after the first pyrolysis, both A_FeNC_H1 and E_FeNC_H1 have nearly similar degrees of defects; however, the samples acquired at later stages, E_FeNC_E and E_FeNC_H2 have a higher I_D/I_G ratio, confirming superior defect density compared to A_FeNC_E and A_FeNC_H2, respectively.

The textural characteristics of the samples acquired at the final stage (H2) were analyzed using BET analysis with nitrogen as an adsorbate. The adsorption/desorption isotherms along with the pore size distribution for both variants, i.e., A_FeNC_H2 and E_FeNC_H2 are illustrated in Figure 5.

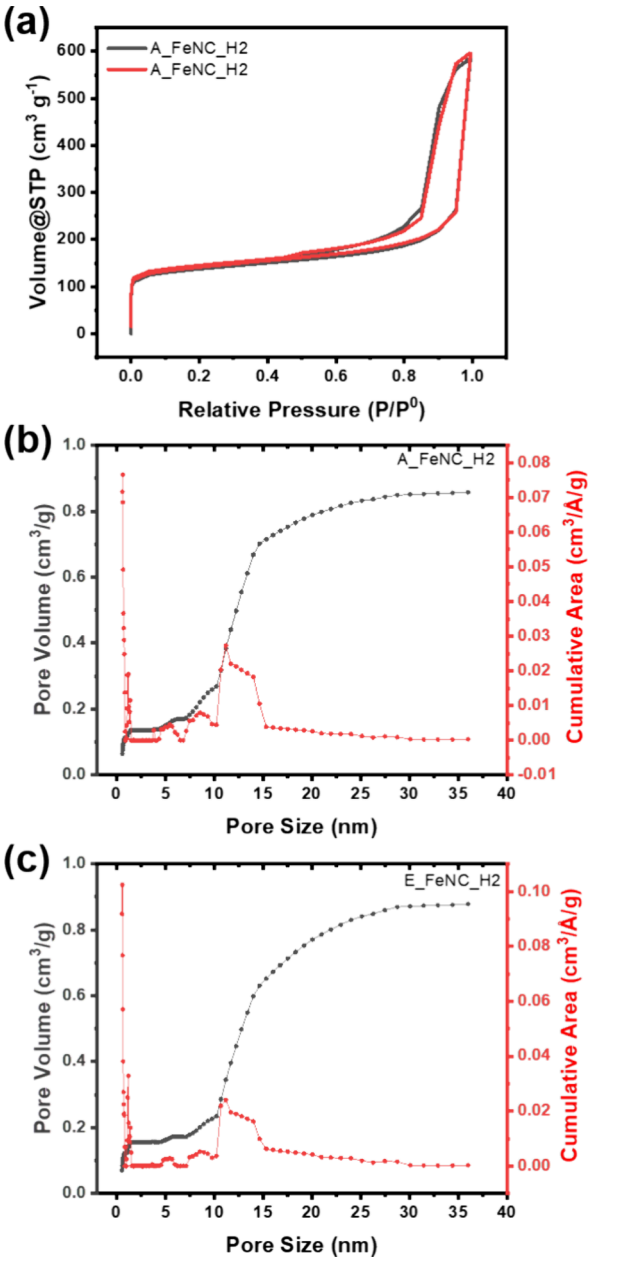

Figure 5. BET nitrogen adsorption−desorption isotherms (a) and pore size distribution (b, c) of the samples acquired after the second pyrolysis stage.

Quite interestingly, the adsorption curves of A_FeNC_H2 and E_FeNC_H2 (Figure 5a) exhibited sudden inflation at very low relative pressure which could be linked with the initial filling of the micropores[61,62] whereas a high proportion of micropores can be found in these samples as indicated in Figure 5b,c. However, the hysteresis loop at higher relative pressure was established as type IV, signifying the presence of cylindrical mesopores according to the classification of the International Union of Pure and Applied Chemistry (IUPAC).[63] Both samples revealed substantial mesoporosity within the 5 to 15 nm range, whereas the estimated BET

https://doi.org/10.1021/acsaem.4c01215
ACS Appl. Energy Mater. XXXX, XXX, XXX−XXX

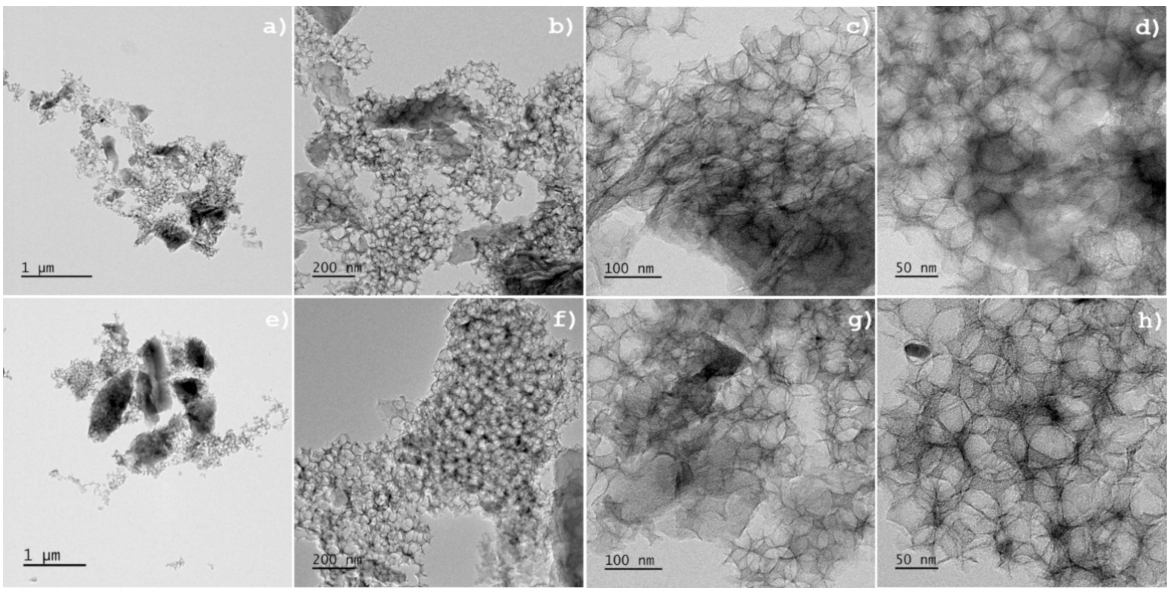

Figure 6. TEM images of (a, d) A_FeNC_H2 and (e–h) E_FeNC_H2.

surface area came out to be 570 and 627 m^2 g^{-1} for A_FeNC_H2 and E_FeNC_H2, respectively. The porosity data acquired through BET has been summarized in Table S3.

Employing TEM the morphological parameters of A_FeNC_H2 and E_FeNC_H2 were investigated. Both samples are constituted of graphitic domains combined with defective carbon-based hollow structures, resulting from the removal of silica NPs (Figure 6). This porous architecture appears slightly more recurrent in the E_FeNC_H2 sample (Figure 6e–g), which correlates well with its higher surface area and higher catalytic activity. The increased porosity likely provides more active sites for the reactions, enhancing its performance. It is important to underline here that, the evolution of iron metallic NPs was not observed in the microstructural study through HRTEM. Where graphitic carbon improves electronic conductivity, the structural defects categorically enhance the ORR electrocatalysis by exposing the numerous active sites.[64]

Along with morphology and structural attributes, surface chemistry plays a pivotal role in ORR electrocatalysis where multitudes of active moieties situated at different site locations distinctly contribute to the reaction pathway and kinetics.[9,16] Therefore, the enrichment and accessibility of the most active and robust moieties are the main goals of electrocatalyst engineering. Therefore, to verify the presence of the active sites of interest, XPS analysis was carried out on the best-performing electrocatalysts achieved at the final stage of the experimental design, and the recorded survey scan is presented in Figure S7. To index the active moieties, the high-resolution N 1s and Fe 2p spectra of A_FeNC_H2 and E_FeNC_H2 were recorded. Besides the envisaged presence of the features of Fe^{2+} species in the Fe 2p spectrum (Figure S8), the most important information comes from the deconvolution of the N 1s spectral region (Figure 7). Almost all the essential N-based active sites, i.e., Fe–N_x, hydrogenated N, pyridinic N, graphitic or protonated N, imine N, and NO_x, were identified by exhibiting peaks at their characteristic binding energy (B.E.) values[14,65–68] and their abundance was calculated and summarized in Figure S9. An appreciable content of Fe–N_x species was detected at their typical B.E. of about 399.6 in both

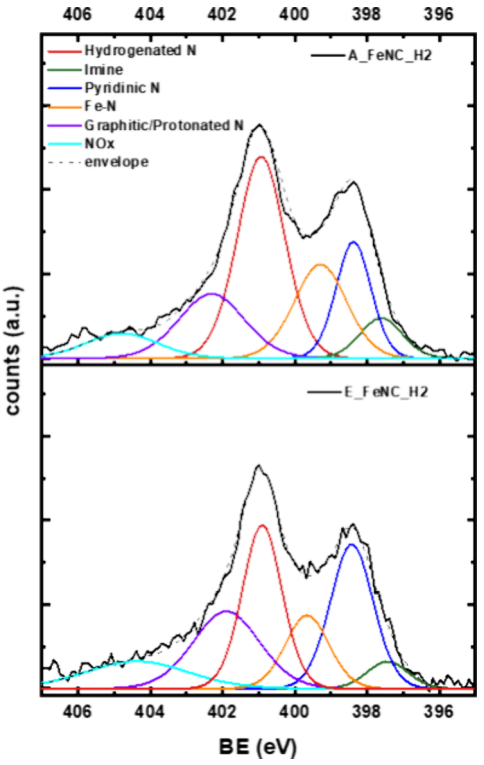

Figure 7. High-resolution XPS N 1S spectra of A_FeNC_H2 and E_FeNC_H2.

samples. It is important to note that Fe–N_x is the primary site to selectively carry out direct 4 electron oxygen electroreduction[16] which is primarily important for fuel cell applications to deliver higher conversion efficiency while generating water as the safe final product, whereas the generation of reactive peroxide radicals via bielectronic ORR may severely affect the fuel cell performance.[69] Moreover, both electrocatalysts exhibited the noticeable pyridinic N and hydrogenated N indicated by categorically intense peaks; however, the relatively lower content of graphitic N was witnessed for both samples. Here, it is important to underline

https://doi.org/10.1021/acsaem.4c01215
ACS Appl. Energy Mater. XXXX, XXX, XXX–XXX

that hydrogenated N (both pyrrolic and hydrogenated pyridine) stepwise reduces oxygen in the 2 + 2 electron pathway while pyridinic N can effectively act as a secondary site to further reduce the already produced peroxides into water and complete the reaction.[14,16,65] Therefore, the higher proportion of these two types of active sites is also indispensable in addition to Fe−N_x for the complete ORR. On the other hand, the presence of graphitic N not only leads to a higher yield of unwanted peroxide due to incomplete ORR but also affects the performance parameters.[14,60] Santoro et al. have already observed that the presence of nitrogen, particularly as Fe−N_x and pyridinic N directly contributes to higher power densities of fuel cells, on the other hand, graphitic N deteriorates the performance.[70]

It has previously been discussed that the electrocatalytic performances of the electrocatalysts increase as the fabrication steps are followed, which indicates the efficacy of the adopted strategy to ultimately develop efficient Fe−N_x−C architecture with accessible active sites of various natures. To certify this observation, the structural features of the fabricated electrocatalysts were thoroughly analyzed. The samples acquired at the final stage of the synthesis route demonstrated the best electrocatalytic performance which can be attributed to such structural features. The morphological investigation through HRTEM confirmed a combination of defective/amorphous and graphitic domains with the absence of Fe coalescence into NPs. This observation was further endorsed by the XRD pattern which shows broader peaks consistent with defective carbon while the peaks corresponding to any crystalline or metallic phase were not observed. Superior defect density for E_FeNC_H2 was also verified by Raman spectroscopy in addition to HRTEM. Similarly, higher surface areas with micromesoporous profiles verified via BET could help provide an easy path to the active sites, whereas the surface area of E_FeNC_H2 (627 m^2 g^{-1}) came out to be higher than A_FeNC_H2. It is important to recall that the sample E_FeNC_H2 not only exhibited slightly higher E_{onset} in both acidic and alkaline media but also the peroxide yield of E_FeNC_H2 was lower compared to A_FeNC_H2. This could be ascribed to the better accessibility of the active sites in E_FeNC_H2. Moreover, XPS additionally illustrated the suitable surface chemistry with the presence of nitrogen-based species of interest. Although the sample E_FeNC_H2 showed a relatively lower proportion of Fe−N_x compared to A_FeNC_H2, much higher pyridinic and enough hydrogenated N (Figure S9) with good accessibility could be a reason behind the nearly four-electron pathway. Furthermore, the graphitic N known for the peroxide yield and increasing the overpotential was much higher in A_FeNC_H2 while in E_FeNC_H2 it was negligible. A comparison of the ORR activity for several recently reported electrocatalysts developed by varying templating methodologies has been presented in Table S4.

CONCLUSIONS

In this study, a novel pathway to engineer the Fe−N_x−C active site structure was presented through a modified SSM methodology. First silica NPs of 70 nm were developed using the traditional Stober process and then functionalized with atomic Fe using two different salines; APTES and EDTMS. The obtained functionalized templates, i.e., Si_AFe and Si_EFe were impregnated with nicarbazin which is an important nitrogen and carbon precursor followed by subjecting to pyrolysis (H1) at 900 °C under an inert atmosphere. Afterward, to remove the silica template the pyrolyzed product was etched with an acidic solution and then again submitted to another pyrolysis (H2) treatment under a slightly reducing atmosphere to ensure the better homogenization of the active sites. ORR electrocatalytic activities in acidic and alkaline media were analyzed using the RRDE technique which categorically exhibited advancement in the ORR performance as the experimental design proceeded. The sample acquired at the final stages of A_FeNC_H2 and E_FeNC_H2 outperformed the other counterparts developed at the initial stages. However, E_FeNC_H2 demonstrated remarkable E_{onset} values of 0.99 and 0.86 V vs RHE in 0.1 M KOH and 0.5 M H_2SO_4 electrolytes, respectively. Moreover, the sample showed the lowest peroxide yield with a nearly direct four-electronic pathway. The best performance of E_FeNC_H2 can be attributed to a suitable combination of active sites and higher surface area with a micromesoporous profile.

ASSOCIATED CONTENT

Supporting Information

The Supporting Information is available free of charge at https://pubs.acs.org/doi/10.1021/acsaem.4c01215.

Additional electrocatalyst characterization including TGA profiles, UV−vis spectra, CVs in stationary conditions, XRD spectra, Raman spectra, EDX spectra, XPS spectra, and durability tests (PDF)

AUTHOR INFORMATION

Corresponding Authors

Massimiliano D'Arienzo − *Department of Materials Science, University of Milano-Bicocca, 20125 Milano, Italy;* orcid.org/0000-0002-5291-9858; Email: massimiliano.darienzo@unimib.it

Carlo Santoro − *Department of Materials Science, University of Milano-Bicocca, 20125 Milano, Italy;* orcid.org/0000-0002-0944-4500; Email: carlo.santoro@unimib.it

Authors

Mohsin Muhyuddin − *Department of Materials Science, University of Milano-Bicocca, 20125 Milano, Italy*

Silvia Mostoni − *Department of Materials Science, University of Milano-Bicocca, 20125 Milano, Italy;* orcid.org/0000-0003-1111-6140

Hilah Clara Honig − *Chemistry Department, Bar-Ilan Center for Nanotechnology and Advanced Materials, Bar-Ilan University, Ramat-Gan 5290002, Israel*

Lorenzo Mirizzi − *Department of Materials Science, University of Milano-Bicocca, 20125 Milano, Italy*

Lior Elbaz − *Chemistry Department, Bar-Ilan Center for Nanotechnology and Advanced Materials, Bar-Ilan University, Ramat-Gan 5290002, Israel;* orcid.org/0000-0003-4989-5135

Roberto Scotti − *Department of Materials Science, University of Milano-Bicocca, 20125 Milano, Italy; Institute for Photonics and Nanotechnologies-CNR, 38123 Trento, TN, Italy*

Complete contact information is available at: https://pubs.acs.org/10.1021/acsaem.4c01215

https://doi.org/10.1021/acsaem.4c01215
ACS Appl. Energy Mater. XXXX, XXX, XXX−XXX

Author Contributions

[‖]M.M., S.M., and H.C.H. have equally contributed to the manuscript.

Notes

The authors declare no competing financial interest.

■ ACKNOWLEDGMENTS

C.S. and L.E. would like to acknowledge the Italian Ministry of Foreign Affairs and International Cooperation—Directorate General for Cultural and Economic Promotion and Innovation (Italian Republic) and the Israel Ministry of Science and Technology within the bilateral project Italy-Israel (WE-CAT).

■ REFERENCES

(1) Zaman, S.; Huang, L.; Douka, A. I.; Yang, H.; You, B.; Xia, B. Y. Oxygen Reduction Electrocatalysts toward Practical Fuel Cells: Progress and Perspectives. *Angew. Chem., Int. Ed.* **2021**, *60* (33), 17832−17852.

(2) Nie, Y.; Li, L.; Wei, Z. Recent Advancements in Pt and Pt-Free Catalysts for Oxygen Reduction Reaction. *Chem. Soc. Rev.* **2015**, *44* (8), 2168−2201.

(3) Wang, W.; Jia, Q.; Mukerjee, S.; Chen, S. Recent Insights into the Oxygen-Reduction Electrocatalysis of Fe/N/C Materials. *ACS Catal.* **2019**, *9* (11), 10126−10141.

(4) He, Y.; Liu, S.; Priest, C.; Shi, Q.; Wu, G. Atomically Dispersed Metal−Nitrogen−Carbon Catalysts for Fuel Cells: Advances in Catalyst Design, Electrode Performance, and Durability Improvement. *Chem. Soc. Rev.* **2020**, *49* (11), 3484−3524.

(5) Jasinski, R. A New Fuel Cell Cathode Catalyst. *Nature* **1964**, *201* (4925), 1212−1213.

(6) Sarapuu, A.; Lilloja, J.; Akula, S.; Zagal, J. H.; Specchia, S.; Tammeveski, K. Recent Advances in Non-Precious Metal Single-Atom Electrocatalysts for Oxygen Reduction Reaction in Low-Temperature Polymer-Electrolyte Fuel Cells. *ChemCatChem.* **2023**, *15* (22), No. e202300849.

(7) Hossen, M. M.; Hasan, M. S.; Sardar, M. R. I.; Haider, J. b.; Mottakin; Tammeveski, K.; Atanassov, P. State-of-the-Art and Developmental Trends in Platinum Group Metal-Free Cathode Catalyst for Anion Exchange Membrane Fuel Cell (AEMFC). *Appl. Catal. B Environ.* **2023**, *325*, No. 121733.

(8) Muhyuddin, M.; Mustarelli, P.; Santoro, C. Recent Advances in Waste Plastic Transformation into Valuable Platinum-Group Metal-Free Electrocatalysts for Oxygen Reduction Reaction. *ChemSusChem* **2021**, *14* (18), 3785−3800.

(9) Asset, T.; Atanassov, P. Iron-Nitrogen-Carbon Catalysts for Proton Exchange Membrane Fuel Cells. *Joule* **2020**, *4* (1), 33−44.

(10) Fauzi, A.; Chen, X.; Zhao, H.; Cao, S.; Kong, L.; Huang, S.; Zhang, S.; Ma, X. Recent Progress of M-N-C Single Atom Electrocatalysts for Carbon Dioxide Reduction Reaction. *Next Energy* **2023**, *1* (4), No. 100045.

(11) Snitkoff-Sol, R. Z.; Friedman, A.; Honig, H. C.; Yurko, Y.; Kozhushner, A.; Zachman, M. J.; Zelenay, P.; Bond, A. M.; Elbaz, L. Quantifying the Electrochemical Active Site Density of Precious Metal-Free Catalysts in Situ in Fuel Cells. *Nat. Catal* **2022**, *5* (2), 163−170.

(12) Snitkoff-Sol, R. Z.; Rimon, O.; Bond, A. M.; Elbaz, L. Direct Measurement of the Oxygen Reduction Reaction Kinetics on Iron Phthalocyanine Using Advanced Transient Voltammetry. *Nat. Catal* **2024**, *7* (2), 139−147.

(13) Snitkoff-Sol, R. Z.; Elbaz, L. Assessing and Measuring the Active Site Density of PGM-Free ORR Catalysts. *J. Solid State Electrochem* **2022**, *26* (9), 1839−1850.

(14) Kabir, S.; Artyushkova, K.; Serov, A.; Atanassov, P. Role of Nitrogen Moieties in N-Doped 3D-Graphene Nanosheets for Oxygen Electroreduction in Acidic and Alkaline Media. *ACS Appl. Mater. Interfaces* **2018**, *10* (14), 11623−11632.

(15) Zhong, W.; Wang, Z.; Han, S.; Deng, L.; Yu, J.; Lin, Y.; Long, X.; Gu, M.; Yang, S. Identifying the Active Sites of a Single Atom Catalyst with pH-Universal Oxygen Reduction Reaction Activity. *Cell Rep. Phys. Sci.* **2020**, *1* (7), No. 100115.

(16) Artyushkova, K.; Serov, A.; Rojas-Carbonell, S.; Atanassov, P. Chemistry of Multitudinous Active Sites for Oxygen Reduction Reaction in Transition Metal−Nitrogen−Carbon Electrocatalysts. *J. Phys. Chem. C* **2015**, *119* (46), 25917−25928.

(17) Chen, M.-X.; Tong, L.; Liang, H.-W. Understanding the Catalytic Sites of Metal−Nitrogen−Carbon Oxygen Reduction Electrocatalysts. *Chem.—Eur. J.* **2021**, *27* (1), 145−157.

(18) Persky, Y.; Kielesiński, Ł.; Reddy, S. N.; Zion, N.; Friedman, A.; Honig, H. C.; Koszarna, B.; Zachman, M. J.; Grinberg, I.; Gryko, D. T.; Elbaz, L. Biomimetic Fe−Cu Porphyrrole Aerogel Electrocatalyst for Oxygen Reduction Reaction. *ACS Catal.* **2023**, *13* (16), 11012−11022.

(19) Wagner, S.; Auerbach, H.; Tait, C. E.; Martinaiou, I.; Kumar, S. C. N.; Kübel, C.; Sergeev, I.; Wille, H.-C.; Behrends, J.; Wolny, J. A.; Schünemann, V.; Kramm, U. I. Elucidating the Structural Composition of an Fe−N−C Catalyst by Nuclear- and Electron-Resonance Techniques. *Angew. Chem., Int. Ed.* **2019**, *58* (31), 10486−10492.

(20) Kneebone, J. L.; Daifuku, S. L.; Kehl, J. A.; Wu, G.; Chung, H. T.; Hu, M. Y.; Alp, E. E.; More, K. L.; Zelenay, P.; Holby, E. F.; Neidig, M. L. A Combined Probe-Molecule, Mössbauer, Nuclear Resonance Vibrational Spectroscopy, and Density Functional Theory Approach for Evaluation of Potential Iron Active Sites in an Oxygen Reduction Reaction Catalyst. *J. Phys. Chem. C* **2017**, *121* (30), 16283−16290.

(21) Freitas, W. d. S.; D'Epifanio, A.; Ficca, V. C. A.; Placidi, E.; Arciprete, F.; Mecheri, B. Tailoring Active Sites of Iron-Nitrogen-Carbon Catalysts for Oxygen Reduction in Alkaline Environment: Effect of Nitrogen-Based Organic Precursor and Pyrolysis Atmosphere. *Electrochim. Acta* **2021**, *391*, No. 138899.

(22) Xue, J.; Zhao, L.; Dou, Z.; Yang, Y.; Guan, Y.; Zhu, Z.; Cui, L. Nitrogen-Doped 3D Porous Carbons with Iron Carbide Nanoparticles Encapsulated in Graphitic Layers Derived from Functionalized MOF as an Efficient Noble-Metal-Free Oxygen Reduction Electrocatalysts in Both Acidic and Alkaline Media. *RSC Adv.* **2016**, *6* (112), 110820−110830.

(23) Persky, Y.; Yurko, Y.; Snitkoff-Sol, R. Z.; Zion, N.; Elbaz, L. Tuning the Performance of Fe−Porphyrin Aerogel-Based PGM-Free Oxygen Reduction Reaction Catalysts in Proton Exchange Membrane Fuel Cells. *Nanoscale* **2023**, *16* (1), 438−446.

(24) Akula, S.; Mooste, M.; Zulevi, B.; McKinney, S.; Kikas, A.; Piirsoo, H.-M.; Rähn, M.; Tamm, A.; Kisand, V.; Serov, A.; Creel, E. B.; Cullen, D. A.; Neyerlin, K. C.; Wang, H.; Odgaard, M.; Reshetenko, T.; Tammeveski, K. Mesoporous Textured Fe-N-C Electrocatalysts as Highly Efficient Cathodes for Proton Exchange Membrane Fuel Cells. *J. Power Sources* **2022**, *520*, No. 230819.

(25) Lilloja, J.; Mooste, M.; Kibena-Põldsepp, E.; Sarapuu, A.; Zulevi, B.; Kikas, A.; Piirsoo, H.-M.; Tamm, A.; Kisand, V.; Holdcroft, S.; Serov, A.; Tammeveski, K. Mesoporous Iron-Nitrogen Co-Doped Carbon Material as Cathode Catalyst for the Anion Exchange Membrane Fuel Cell. *J. Power Sources Adv.* **2021**, *8*, No. 100052.

(26) Kramm, U. I.; Lefèvre, M.; Larouche, N.; Schmeisser, D.; Dodelet, J.-P. Correlations between Mass Activity and Physicochemical Properties of Fe/N/C Catalysts for the ORR in PEM Fuel Cell via 57Fe Mössbauer Spectroscopy and Other Techniques. *J. Am. Chem. Soc.* **2014**, *136* (3), 978−985.

(27) Jaouen, F.; Lefèvre, M.; Dodelet, J.-P.; Cai, M. Heat-Treated Fe/N/C Catalysts for O2 Electroreduction: Are Active Sites Hosted in Micropores? *J. Phys. Chem. B* **2006**, *110* (11), 5553−5558.

(28) Kim, M.; Kim, H. S.; Yoo, S. J.; Yoo, W. C.; Sung, Y.-E. The Role of Pre-Defined Microporosity in Catalytic Site Formation for the Oxygen Reduction Reaction in Iron- and Nitrogen-Doped Carbon Materials. *J. Mater. Chem. A* **2017**, *5* (8), 4199−4206.

(29) Kaneti, Y. V.; Dutta, S.; Hossain, Md. S. A.; Shiddiky, M. J. A.; Tung, K.-L.; Shieh, F.-K.; Tsung, C.-K.; Wu, K. C.-W.; Yamauchi, Y.

https://doi.org/10.1021/acsaem.4c01215
ACS Appl. Energy Mater. XXXX, XXX, XXX−XXX

Strategies for Improving the Functionality of Zeolitic Imidazolate Frameworks: Tailoring Nanoarchitectures for Functional Applications. *Adv. Mater.* **2017**, *29* (38), No. 1700213.
(30) Kumar, K.; Asset, T.; Li, X.; Liu, Y.; Yan, X.; Chen, Y.; Mermoux, M.; Pan, X.; Atanassov, P.; Maillard, F.; Dubau, L. Fe−N−C Electrocatalysts' Durability: Effects of Single Atoms' Mobility and Clustering. *ACS Catal.* **2021**, *11* (2), 484−494.
(31) Yarlagadda, V.; Carpenter, M. K.; Moylan, T. E.; Kukreja, R. S.; Koestner, R.; Gu, W.; Thompson, L.; Kongkanand, A. Boosting Fuel Cell Performance with Accessible Carbon Mesopores. *ACS Energy Lett.* **2018**, *3* (3), 618−621.
(32) Han, X.; Zhang, T.; Wang, X.; Zhang, Z.; Li, Y.; Qin, Y.; Wang, B.; Han, A.; Liu, J. Hollow Mesoporous Atomically Dispersed Metal-Nitrogen-Carbon Catalysts with Enhanced Diffusion for Catalysis Involving Larger Molecules. *Nat. Commun.* **2022**, *13* (1), 2900.
(33) Mazzucato, M.; Daniel, G.; Mehmood, A.; Kosmala, T.; Granozzi, G.; Kucernak, A.; Durante, C. Effects of the Induced Micro- and Meso-Porosity on the Single Site Density and Turn over Frequency of Fe-N-C Carbon Electrodes for the Oxygen Reduction Reaction. *Appl. Catal. B Environ.* **2021**, *291*, No. 120068.
(34) Serov, A.; Artyushkova, K.; Niangar, E.; Wang, C.; Dale, N.; Jaouen, F.; Sougrati, M.-T.; Jia, Q.; Mukerjee, S.; Atanassov, P. Nano-Structured Non-Platinum Catalysts for Automotive Fuel Cell Application. *Nano Energy* **2015**, *16*, 293−300.
(35) *Pajarito Powder*. https://pajaritopowder.com/ (accessed 2024−03−03).
(36) Kisand, K.; Sarapuu, A.; Douglin, J. C.; Kikas, A.; Treshchalov, A.; Käärik, M.; Piirsoo, H.-M.; Paiste, P.; Aruväli, J.; Leis, J.; Kisand, V.; Tamm, A.; Dekel, D. R.; Tammeveski, K. Templated Nitrogen-, Iron-, and Cobalt-Doped Mesoporous Nanocarbon Derived from an Alkylresorcinol Mixture for Anion-Exchange Membrane Fuel Cell Application. *ACS Catal.* **2022**, *12* (22), 14050−14061.
(37) Sajjad, U.; Sarapuu, A.; Douglin, J. C.; Kikas, A.; Treshchalov, A.; Käärik, M.; Kozlova, J.; Aruväli, J.; Leis, J.; Kisand, V.; Kukli, K.; Dekel, D. R.; Tammeveski, K. Lignin-Derived Precious Metal-Free Electrocatalysts for Anion-Exchange Membrane Fuel Cell Application. *ACS Catal.* **2024**, *14* (12), 9224−9234.
(38) Mazzucato, M.; Daniel, G.; Perazzolo, V.; Brandiele, R.; Rizzi, G. A.; Isse, A. A.; Gennaro, A.; Durante, C. Mesoporosity and Nitrogen Doping: The Leading Effect in Oxygen Reduction Reaction Activity and Selectivity at Nitrogen-Doped Carbons Prepared by Using Polyethylene Oxide-Block-Polystyrene as a Sacrificial Template. *Electrochem. Sci. Adv.* **2023**, *3* (2), No. e2100203.
(39) Zhang, Z.; Jiang, W.; Long, D.; Wang, J.; Qiao, W.; Ling, L. A General Silica-Templating Synthesis of Alkaline Mesoporous Carbon Catalysts for Highly Efficient H2S Oxidation at Room Temperature. *ACS Appl. Mater. Interfaces* **2017**, *9* (3), 2477−2484.
(40) Tong, L.; Wang, Y.-C.; Chen, M.-X.; Chen, Z.-Q.; Yan, Q.-Q.; Yang, C.-L.; Zhou, Z.-Y.; Chu, S.-Q.; Feng, X.; Liang, H.-W. Hierarchically Porous Carbons as Supports for Fuel Cell Electrocatalysts with Atomically Dispersed Fe−Nx Moieties. *Chem. Sci.* **2019**, *10* (35), 8236−8240.
(41) Miao, Z.; Wang, X.; Tsai, M.-C.; Jin, Q.; Liang, J.; Ma, F.; Wang, T.; Zheng, S.; Hwang, B.-J.; Huang, Y.; Guo, S.; Li, Q. Atomically Dispersed Fe-Nx/C Electrocatalyst Boosts Oxygen Catalysis via a New Metal-Organic Polymer Supramolecule Strategy. *Adv. Energy Mater.* **2018**, *8* (24), No. 1801226.
(42) Ariana Mirshokraee, S.; Muhyuddin, M.; Orsilli, J.; Berretti, E.; Capozzoli, L.; Lavacchi, A.; Vecchio, C. L.; Baglio, V.; Galli, A.; Zaffora, A.; Franco, F. D.; Santamaria, M.; Olivi, L.; Pollastri, S.; Santoro, C. Mono-, Bi- and Tri-Metallic Platinum Group Metal-Free Electrocatalysts for Hydrogen Evolution Reaction Following a Facile Synthetic Route. *Ind. Chem. Mater.* **2023**, *1* (3), 343−359.
(43) Ariana Mirshokraee, S.; Muhyuddin, M.; Orsilli, J.; Berretti, E.; Lavacchi, A.; Vecchio, C. L.; Baglio, V.; Viscardi, R.; Zaffora, A.; Franco, F. D.; Santamaria, M.; Olivi, L.; Pollastri, S.; Santoro, C. Mono-, Bi- and Tri-Metallic Fe-Based Platinum Group Metal-Free Electrocatalysts Derived from Phthalocyanine for Oxygen Reduction Reaction in Alkaline Media. *Nanoscale* **2024**, *16* (13), 6531−6547.
(44) Mathur, A.; Harish, S.; Halder, A. Role of Nitrogen Precursor on the Activity Descriptor towards Oxygen Reduction Reaction in Iron-Based Catalysts. *ChemistrySelect* **2018**, *3* (23), 6542−6550.
(45) Huang, Y.; Chen, Y.; Xu, M.; Asset, T.; Tieu, P.; Gili, A.; Kulkarni, D.; De Andrade, V.; De Carlo, F.; Barnard, H. S.; Doran, A.; Parkinson, D. Y.; Pan, X.; Atanassov, P.; Zenyuk, I. V. Catalysts by Pyrolysis: Direct Observation of Chemical and Morphological Transformations Leading to Transition Metal-Nitrogen-Carbon Materials. *Mater. Today* **2021**, *47*, 53−68.
(46) Kübler, M.; Wagner, S.; Jurzinsky, T.; Paul, S.; Weidler, N.; Gomez Villa, E. D.; Cremers, C.; Kramm, U. I. Impact of Surface Functionalization on the Intrinsic Properties of the Resulting Fe−N−C Catalysts for Fuel Cell Applications. *Energy Technol.* **2020**, *8* (9), 2000433.
(47) Stöber, W.; Fink, A.; Bohn, E. Controlled Growth of Monodisperse Silica Spheres in the Micron Size Range. *J. Colloid Interface Sci.* **1968**, *26* (1), 62−69.
(48) Mezzomo, L.; Bonato, S.; Mostoni, S.; Credico, B. D.; Scotti, R.; D'Arienzo, M.; Mustarelli, P.; Ruffo, R. Composite Solid-State Electrolyte Based on Hybrid Poly(Ethylene Glycol)-Silica Fillers Enabling Long-Life Lithium Metal Batteries. *Electrochim. Acta* **2022**, *411*, No. 140060.
(49) Mostoni, S.; D'Arienzo, M.; Di Credico, B.; Armelao, L.; Rancan, M.; Dirè, S.; Callone, E.; Donetti, R.; Susanna, A.; Scotti, R. Design of a Zn Single-Site Curing Activator for a More Sustainable Sulfur Cross-Link Formation in Rubber. *Ind. Eng. Chem. Res.* **2021**, *60* (28), 10180−10192.
(50) Muhyuddin, M.; Filippi, J.; Zoia, L.; Bonizzoni, S.; Lorenzi, R.; Berretti, E.; Capozzoli, L.; Bellini, M.; Ferrara, C.; Lavacchi, A.; Santoro, C. Waste Face Surgical Mask Transformation into Crude Oil and Nanostructured Electrocatalysts for Fuel Cells and Electrolyzers. *ChemSusChem* **2022**, *15* (2), No. e202102351.
(51) Testa, D.; Zuccante, G.; Muhyuddin, M.; Landone, R.; Scommegna, A.; Lorenzi, R.; Acciarri, M.; Petri, E.; Soavi, F.; Poggini, L.; Capozzoli, L.; Lavacchi, A.; Lamanna, N.; Franzetti, A.; Zoia, L.; Santoro, C. Giving New Life to Waste Cigarette Butts: Transformation into Platinum Group Metal-Free Electrocatalysts for Oxygen Reduction Reaction in Acid, Neutral and Alkaline Environment. *Catalysts* **2023**, *13* (3), 635.
(52) Giordano, E.; Berretti, E.; Capozzoli, L.; Lavacchi, A.; Muhyuddin, M.; Santoro, C.; Gatto, I.; Zaffora, A.; Santamaria, M. Boosting DMFC Power Output by Adding Sulfuric Acid as a Supporting Electrolyte: Effect on Cell Performance Equipped with Platinum and Platinum Group Metal-Free Cathodes. *J. Power Sources* **2023**, *563*, No. 232806.
(53) Chen, Y.; Huang, Y.; Xu, M.; Asset, T.; Yan, X.; Artyushkova, K.; Kodali, M.; Murphy, E.; Ly, A.; Pan, X.; Zenyuk, I. V.; Atanassov, P. Catalysts by Pyrolysis: Direct Observation of Transformations during Re-Pyrolysis of Transition Metal-Nitrogen-Carbon Materials Leading to State-of-the-Art Platinum Group Metal-Free Electrocatalyst. *Mater. Today* **2022**, *53*, 58−70.
(54) Muhyuddin, M.; Friedman, A.; Poli, F.; Petri, E.; Honig, H.; Basile, F.; Fasolini, A.; Lorenzi, R.; Berretti, E.; Bellini, M.; Lavacchi, A.; Elbaz, L.; Santoro, C.; Soavi, F. Lignin-Derived Bimetallic Platinum Group Metal-Free Oxygen Reduction Reaction Electrocatalysts for Acid and Alkaline Fuel Cells. *J. Power Sources* **2023**, *556*, No. 232416.
(55) Brocato, S.; Serov, A.; Atanassov, P. pH Dependence of Catalytic Activity for ORR of the Non-PGM Catalyst Derived from Heat-Treated Fe−Phenanthroline. *Electrochim. Acta* **2013**, *87*, 361−365.
(56) Ramaswamy, N.; Mukerjee, S. Fundamental Mechanistic Understanding of Electrocatalysis of Oxygen Reduction on Pt and Non-Pt Surfaces: Acid versus Alkaline Media. *Adv. Phys. Chem.* **2012**, *2012*, No. 491604.
(57) Pasternack, R. M.; Rivillon Amy, S.; Chabal, Y. J. Attachment of 3-(Aminopropyl)Triethoxysilane on Silicon Oxide Surfaces: Dependence on Solution Temperature. *Langmuir* **2008**, *24* (22), 12963−12971.

https://doi.org/10.1021/acsaem.4c01215
ACS Appl. Energy Mater. XXXX, XXX, XXX−XXX

(58) Zhu, C.; Shi, Q.; Xu, B. Z.; Fu, S.; Wan, G.; Yang, C.; Yao, S.; Song, J.; Zhou, H.; Du, D.; Beckman, S. P.; Su, D.; Lin, Y. Hierarchically Porous M−N−C (M = Co and Fe) Single-Atom Electrocatalysts with Robust MNx Active Moieties Enable Enhanced ORR Performance. *Adv. Energy Mater.* **2018**, *8* (29), No. 1801956.
(59) Luo, X.; Wei, X.; Wang, H.; Gu, W.; Kaneko, T.; Yoshida, Y.; Zhao, X.; Zhu, C. Secondary-Atom-Doping Enables Robust Fe−N−C Single-Atom Catalysts with Enhanced Oxygen Reduction Reaction. *Nano-Micro Lett.* **2020**, *12* (1), 163.
(60) Muhyuddin, M.; Berretti, E.; Mirshokraee, S. A.; Orsilli, J.; Lorenzi, R.; Capozzoli, L.; D'Acapito, F.; Murphy, E.; Guo, S.; Atanassov, P.; Lavacchi, A.; Santoro, C. Formation of the Active Site Structures during Pyrolysis Transformation of Fe-Phthalocyanine into Fe-Nx-C Electrocatalysts for the Oxygen Reduction Reaction. *Appl. Catal. B Environ.* **2024**, *343*, No. 123515.
(61) Muhyuddin, M.; Testa, D.; Lorenzi, R.; Vanacore, G. M.; Poli, F.; Soavi, F.; Specchia, S.; Giurlani, W.; Innocenti, M.; Rosi, L.; Santoro, C. Iron-Based Electrocatalysts Derived from Scrap Tires for Oxygen Reduction Reaction: Evolution of Synthesis-Structure-Performance Relationship in Acidic. *Neutral and Alkaline Media. Electrochim. Acta* **2022**, *433*, No. 141254.
(62) Bchellaoui, N.; Hayat, Z.; Mami, M.; Rachida, D.-S.; El Abed, A. Microfluidic-Assisted Formation of Highly Monodisperse and Mesoporous Silica Soft Microcapsules. *Sci. Rep.* **2017**, *7*, 16326.
(63) Sing, K. Reporting Physisorption Data for Gas/Solid Systems with Special Reference to the Determination of Surface Area and Porosity. *Pure Appl. Chem.* **1982**, *54*, 2201−2218.
(64) Yan, D.; Li, Y.; Huo, J.; Chen, R.; Dai, L.; Wang, S. Defect Chemistry of Nonprecious-Metal Electrocatalysts for Oxygen Reactions. *Adv. Mater.* **2017**, *29* (48), No. 1606459.
(65) Chen, Y.; Matanović, I.; Weiler, E.; Atanassov, P.; Artyushkova, K. Mechanism of Oxygen Reduction Reaction on Transition Metal-Nitrogen-Carbon Catalysts: Establishing the Role of Nitrogen-Containing Active Sites. *ACS Appl. Energy Mater.* **2018**, *1*, 5948−5953.
(66) Artyushkova, K. Misconceptions in Interpretation of Nitrogen Chemistry from X-Ray Photoelectron Spectra. *J. Vac. Sci. Technol. A* **2020**, *38* (3), No. 031002.
(67) Lazar, P.; Mach, R.; Otyepka, M. Spectroscopic Fingerprints of Graphitic, Pyrrolic, Pyridinic, and Chemisorbed Nitrogen in N-Doped Graphene. *J. Phys. Chem. C* **2019**, *123* (16), 10695−10702.
(68) Zuccante, G.; Muhyuddin, M.; Ficca, V. C. A.; Placidi, E.; Acciarri, M.; Lamanna, N.; Franzetti, A.; Zoia, L.; Bellini, M.; Berretti, E.; Lavacchi, A.; Santoro, C. Transforming Cigarette Wastes into Oxygen Reduction Reaction Electrocatalyst: Does Each Component Behave Differently? An Experimental Evaluation. *ChemElectroChem.* **2024**, *11*, No. e202300725.
(69) Wallnöfer-Ogris, E.; Poimer, F.; Köll, R.; Macherhammer, M.-G.; Trattner, A. Main Degradation Mechanisms of Polymer Electrolyte Membrane Fuel Cell Stacks−Mechanisms, Influencing Factors, Consequences, and Mitigation Strategies. *Int. J. Hydrog. Energy* **2024**, *50*, 1159−1182.
(70) Santoro, C.; Serov, A.; Gokhale, R.; Rojas-Carbonell, S.; Stariha, L.; Gordon, J.; Artyushkova, K.; Atanassov, P. A Family of Fe-N-C Oxygen Reduction Electrocatalysts for Microbial Fuel Cell (MFC) Application: Relationships between Surface Chemistry and Performances. *Appl. Catal. B Environ.* **2017**, *205*, 24−33.

https://doi.org/10.1021/acsaem.4c01215
ACS Appl. Energy Mater. XXXX, XXX, XXX−XXX